Journal of
Marine Science and Engineering

MDPI

Article

Field Measurements of a High-Energy Headland Deflection Rip Current: Tidal Modulation, Very Low Frequency Pulsation and Vertical Structure

Damien Sous [1,2,*], Bruno Castelle [3], Arthur Mouragues [3] and Philippe Bonneton [3]

1 Université de Toulon, Aix Marseille Université, CNRS, IRD, Mediterranean Institute of Oceanography (MIO), 83130 La Garde, France
2 Univ Pau & Pays Adour/E2S UPPA, Chaire HPC-Waves, Laboratoire des Sciences de l'Ingénieur Appliquées a la Méchanique et au Génie Electrique - Fédération IPRA, EA4581, 64600 ANGLET, France
3 CNRS, Université de Bordeaux, UMR EPOC 5805, 33600 Pessac, France; bruno.castelle@u-bordeaux.fr (B.C.); arthur.mouragues@u-bordeaux.fr (A.M.); philippe.bonneton@u-bordeaux.fr (P.B.)
* Correspondence: sous@univ-tln.fr; Tel.: +33-(0)491142109

Received: 2 June 2020; Accepted: 14 July 2020; Published: 18 July 2020

Abstract: Headland rips, sometimes referred to as boundary rips, are rip currents flowing against natural or artificial obstructions extending seaward from the beach, such as headland or groynes. They can be driven either by the deflection of the longshore current against the obstacle or by alongshore variation in breaking wave height due to wave shadowing in the lee of the obstacle. The driving mechanism therefore essentially depends on the angle of wave incidence with respect to the natural or artificial obstruction. We analyze 42 days of velocity profile measurements against a natural headland at the high-energy meso-macrotidal beach of Anglet, southwest France. Measurements were collected in 6.5–10.5-m depth as tide elevation varied, during the autumn–winter period with offshore significant wave height and period ranging 0.9–6 m and 8–16 s, respectively, and the angle of wave incidence ranging from $-20°$ to $20°$. Here we analyze deflection rip configurations, corresponding to approximately 24 days of measurements, for which the current meter was alternatively located in the rip neck, rip head or away from the rip as wave and tide conditions changed. Deflection rips were associated with large offshore-directed velocities (up to 0.6 m/s depth-averaged velocities) and tide modulation for low- to moderate-energy waves. The vertical profile of deflection rips was found to vary from depth-uniform in the rip neck to strongly depth-varying further offshore in the rip head with maximum velocities near the surface. Very low frequency motions of the rip were dramatic, ranging 10–60 min with a dominant peak period of approximately 40 min, i.e., with longer periods than commonly reported. The strong offshore-directed velocities measured well beyond the surf zone edge provide new insight into deflection rips as a dominant mechanism for water and sediment exchanges between embayed (or structurally-controlled) beaches and the inner-shelf and/or the adjacent embayments.

Keywords: rip current; headland; current deflection; very low frequency motions; vertical flow structure

1. Introduction

Headland-bay and structurally-controlled beaches are ubiquitous worldwide [1]. Natural or artificial obstruction extending seaward from the coastline can directly impact the incident wave field and, in turn, wave-driven currents (e.g., [2]), sediment transport pathways (e.g., [3]), beach morphodynamics (e.g., [4,5]) and temporal and spatial modes of shoreline variability (e.g., [6,7]). Over the last decades, a lot of efforts have been made to improve our understanding of shoreline change along headland-bay and structurally-controlled beaches. In particular beach rotation, which can

be observed on the scale of individual storm events (e.g., [8]) and more gradually due to seasonal changes in wave conditions (e.g., [9]), has received a lot of attention (e.g., [7,10–14]). By contrast, little is known on the processes affecting large-scale sediment budget of embayed beaches and the underlying processes affecting water and sediment exchanges between the embayed beach and the inner-shelf and/or the adjacent embayments.

In addition to the interruption of and/or trapping of longshore sand transport leading to rotation and breathing modes of shoreline variability [15], headlands are responsible for the presence of potentially intense wave-driven rip currents flowing against them. Such rips have been referred to as topographic rips (e.g., [16]), headland rips (e.g., [17]), and will be hereafter referred to as boundary or headland rips (e.g., [18]). These rip currents are critical to headland sand bypassing, providing sediment connection between adjacent embayed-headland bound beaches [19] and controlling large-scale sand budget and shoreline alignment [20]. In addition, headland rips during severe storms, which are sometimes referred to as mega-rips in such conditions [21–24], can extend very far offshore. These high-energy headland rips have been therefore hypothesized to be the leading mechanism for water/sediment exchange between the nearshore and the inner shelf and therefore for cross-embayment exchange [25,26].

As described in Castelle et al. [18] two distinctly different forcing mechanisms of boundary rip can be discriminated. The mechanism selection depends on which side of the headland waves are coming from (Figure 1). Shadow rips occur on the down-wave side of a rigid boundary (Figure 1a), as the presence of a rigid obstacle results in alongshore variation in wave height and, in turn, alongshore variation in wave energy dissipation due to wave shadowing in the lee of the obstacle. Shadow rip observations are scarce [17,27] and have been carried out in the lee of short obstacles with a sharp and reasonably narrow shadowing zone favoring shadow rip formation. However, natural headlands often show more complex configurations (e.g., extensive length, submerged platform) blurring showing effects. As a result, shadow rips are generally of low energy and are sometimes not observed along the headland [28]. By contrast, *deflection rips* occur on the up-wave side of a boundary (Figure 1b), with a very different driving mechanism. In the case of deflection rips, the alongshore current driven by obliquely incident waves is physically deflected seaward by the obstacle [16,22,29]. Deflection rips are generally more predictable and numerically reproducible than shadow rips [2,16,17,30]. When headland length is larger than 125% of the surf zone width, offshore deflection and exit behavior are maximized as the alongshore current is fully deflected [16]. Compared to other types of rips, deflection rips are typically associated with very high exit rates, often with offshore mean flow pattern extending multiple surf zone widths offshore [18].

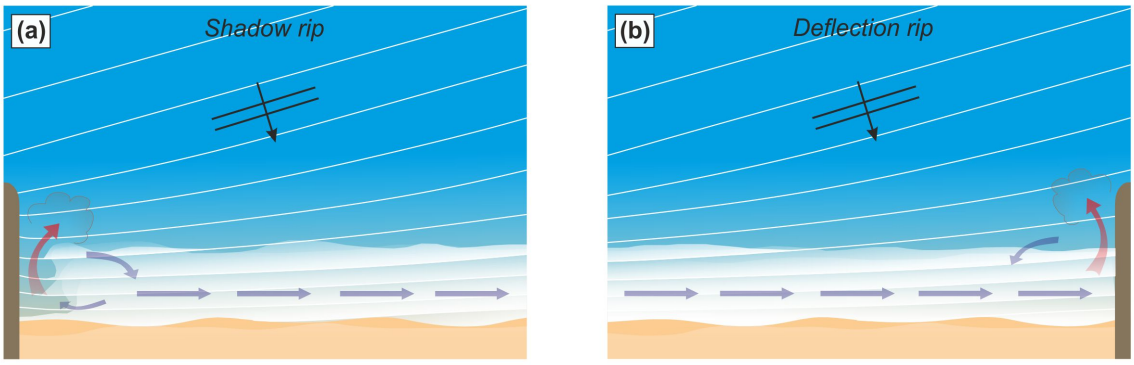

Figure 1. Schematics of the forcing mechanisms driving boundary rips which flow against rigid lateral boundaries such as natural headlands or anthropogenic structures: (**a**) schematic of a shadow rip in the lee of an obstacle (upwave side); (**b**) deflection rip adjacent to obstacle on downwave side of beach.

Deflection rip behavior is therefore critical to our understanding of water and sediment exchanges between the embayed beach and the inner-shelf and/or the adjacent embayments. However, to the best

of our knowledge, there are very few continuous Eulerian flow measurements within the headland rip neck and rip head, and no measurements have been collected during high-energy conditions. One of the two notable exceptions is the unpublished PhD work of Coutts-Smith [21] who deployed current meters during two years offshore an embayed beach in New South Wales, Australia, and captured some high-energy rips, which were assumed as headland rips. The maximum surface flow reached 1.3 m/s in 15-m depth during a severe storm (H_s about 6 m), with typical rip flow pulsing at periods 10–15 min. However, the relationships with an offshore wave and tide conditions were not systematically addressed, and the time-averaging of the velocities was unclear. The second exception is a field experiment that was recently conducted in October 2018 at Anglet beach, southwest France, described in [31] and from which some of the data presented here builds on.

Overall, little is known about the dynamics of deflection rips. Their pulsing characteristics, depth variability and whether they are modulated by the tide like channel rips further away along the beach (e.g., [32–34]), are virtually unknown. This paper aims at paving these knowledge gaps using direct field measurements of headland rip in a high-energy meso-macrotidal beach in southwest France, here focusing on the deflection regime which was well captured by our currentmeter. The present analysis builds on some of the data collected during the experiment presented in Mouragues et al. [31] and on additional measurements subsequently collected at the same beach. In this paper we analyze 42 days of continuous current profiles acquired at 1 Hz in 6.5–10.5 m depth against a natural headland. After analysing rip flow characteristics with regards to bulk wave parameters and tide conditions, an in-depth description of two representative deflection rip events are carried out.

2. Field Experiment

2.1. Field Site

La Petite Chambre d'Amour (PCA) beach is located at the southern end of Anglet beach on the French Basque Coast, southwest France (Figure 2a). It is a high-energy beach exposed to waves generated in the North Atlantic by extra-tropical low-pressure systems tracking eastwards [35]. Waves come primarily from the W-NW direction, and incident wave energy is strongly seasonally modulated, with an annual mean significant wave height and peak period of H_s = 1.57 m (up to 10 m during severe storms) and T_p = 10 s, respectively [36]. The tide regime is mostly composed of semi-diurnal components, giving near-sine oscillations of the Still Water Level (SWL) with an average period of approximately 12 h and 20 minutes. The tidal regime is meso–macro, with tide range varying between 1 and 4.7 m.-macro. Tide-induced currents are weak along the Anglet shores and the waves are by far the dominant, but tidally-modulated, driver of the nearshore hydrodynamics [37]. PCA beach is the most southern stretch of the 4-km long sandy embayment of Anglet, which is bounded by the approximately 500-m long Saint–Martin rocky headland in the south and by the Adour river training wall in the North. In between, six groynes have been implemented over the last decades to constrain shoreline variability. PCA beach is composed of medium to coarse ($D50 \approx 2$ mm) sand with a steep beach face (≈1/10). For more information on Anglet beach setting and beach morphodynamics, the reader is referred to Huguet et al. [38], Rodriguez-Padilla et al. [39].

2.2. Data and Methods

The present dataset gathers the data collected during two successive field deployments: (1) on 8–25 October 2018 in the frame of the large-scale field experiment described in Mouragues et al. [31]; (2) from 16 February to 12 March 2019. In both cases, a single acoustic doppler velocity profiler Nortek Signature 1000 was deployed within the headland rip neck. The headland rip neck location was deduced from the inspection bathymetric surveys prior to the 2018 experiment showing a subtle channel against the headland. In 2018, the instrument was located approximately 70 m from the headland (position 43°29.700′ N, 1°33.210′ W) in approximately 6.5–10.5 m depth depending on the tide elevation (Figure 2b). In 2019, the profiler was mounted 10 m further away from the headland

(43°29.710′ N, 1°33.200′ W) in a similar depth (Figure 2b). The initial intention was to deploy the profiler at the same location for both campaigns but the deployment conditions encountered in 2019 do not allow to safely approach the shore. The small shift between 2018 and 2019 locations should not significantly affect the measurement analysis, in particular in the case of well-developed deflection rips analysis hereafter. For both campaigns, the instrument was deployed on a weighted (150 kg lead) tripod structure. The velocity profile was measured continuously at 1 Hz over 0.2-m cells. The blanking zone was set to 0.1 m. The position of the bottom cell is estimated to approximately 0.65 and 0.3 m above the sand bed at the start and the end of each deployment, respectively.

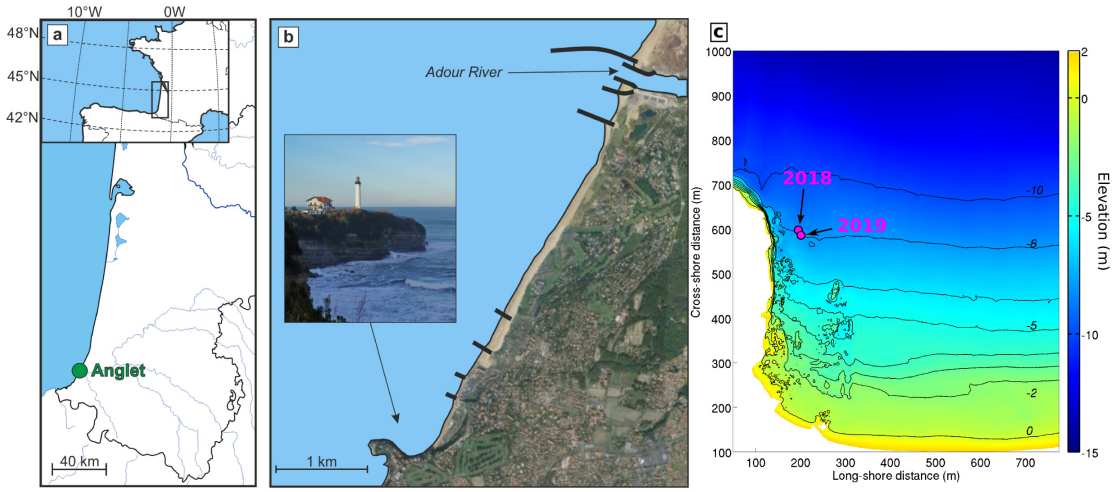

Figure 2. (**a**,**b**) Location map of Anglet beach and Petite Chambre d'Amour beach (PCA), (**c**) nearshore bathymetry with location of the current meters for both deployments (IGN69 referential).

The continuous dataset of 1 Hz velocity profiles was first subdivided into 2-h bursts. While longer duration would have been preferable to increase the number of degrees of freedom, the 2-h duration is the best compromise to capture both the dominant low-frequency fluctuations of the signal and the tidal dependency. On each 2-h burst, the instantaneous velocity profiles were first processed to discard from the analysis cells that were intermittently emerged at the passage of a wave trough. This was carried out by detecting from embedded pressure data the minimal elevation reached during each burst, and restricting the analysis within the water column below this elevation. Velocities were then projected into a cross-shore/alongshore local reference frame: the cross-shore component is aligned with the shore-normal (300° in nautical convention) direction, positive offshore, while the alongshore component is shore-parallel (30° in nautical convention), positive northward:

$$u = u_E \cos(\alpha) + u_N \sin(\alpha) \quad (1)$$

$$v = -u_E \sin(\alpha) + u_N \sin(\alpha), \quad (2)$$

where u_E and u_N are respectively the eastward and northward velocity components provided by the profiler, u and v the alongshore and cross-shore velocity components and α the shore-normal direction (in Nautical convention).

Depth-averaged velocity components, hereafter denoted U and V for the alongshore and cross-shore components, respectively, were computed by averaging the flow velocities from the bottom cell to the surface:

$$U = \frac{1}{N}\sum_{1}^{N} u \quad (3)$$

$$V = \frac{1}{N}\sum_{1}^{N} v \quad (4)$$

where N is the number of immersed cells. A discrete Fourier transform was computed on the depth-averaged velocity components without any windowing to preserve the low-frequency content. The resulting spectra were then smoothed using a 0.00065 Hz moving average. Time-averaged velocity profiles were obtained by averaging the velocity data in each cell either over the complete 2-h burst or using a 2-min moving average in order to low-pass filter out the gravity wave orbital component and to highlight the low frequency pulsations.

Still-water level was obtained from the Bayonne–Boucau tide gauge located near the entrance of the Adour river and operated by the Service Hydrographique and Oceanographique de la Marine (SHOM). Offshore directional wave measurements were collected by an offshore wave buoy moored in approximately 50-m depth offshore of Anglet. In order to relate the offshore wave forcing with the rip development, we computed the longshore wave power P_l defined as:

$$P_l = \rho \frac{g^2}{64\pi} H_s^2 T_e \sin\theta \cos\theta, \tag{5}$$

where ρ is the seawater density, g the gravity acceleration and H_s and T_e are the significant wave height and energetic period (ratio between -1 and 0-order moments of the spectral density) measured at the wave buoy, respectively. The angle of wave incidence θ is positive (negative) for northern (southern) waves, that is, for a wave direction larger (lower) than 300°. The mean direction at the buoy is used for the calculation.

2.3. Field Conditions

Figure 3 depicts the time-series for wave and water level conditions for the two experiments together with the 2-h-averaged and depth-averaged magnitude and direction of the headland rip flow. Overall, for the entire deployments significant wave height H_s ranged from 0.9 to 6 m (Figure 3a,b) and wave period (energetic wave period, T_e) ranged from 8 to 16 s (Figure 3c,d), with larger wave height and period during the 2019 deployment that occurred during winter. Waves came from a relatively narrow W-NW directional window (Figure 3e,f), and more from the W during the 2019 deployment. Accordingly, the longshore power ranges from -25 to 10 kW/m, with more energetic wave events recorded during 2019 (Figure 3g,h), meaning that both shadow rip and deflection rip configurations occurred during the course of the deployments. Overall, the deflection rip regime ($P_l > 0$) was observed during approximately 24 cumulative experiment days. During both deployments, one complete neap-spring tide cycle was covered, with tidal range varying from 1.1 to 3.9 m and from 1.3 to 4.6 m during the first and second deployment, respectively (Figure 3i,j). Wind conditions (not shown) were weak to moderate during both field campaigns, with mean values of approximately 3.0 and 3.7 m/s, respectively, with wind events coming primarily from the W-NW sector. There was no severe storm wind event as the time-averaged wind speed never exceeded 12 m/s.

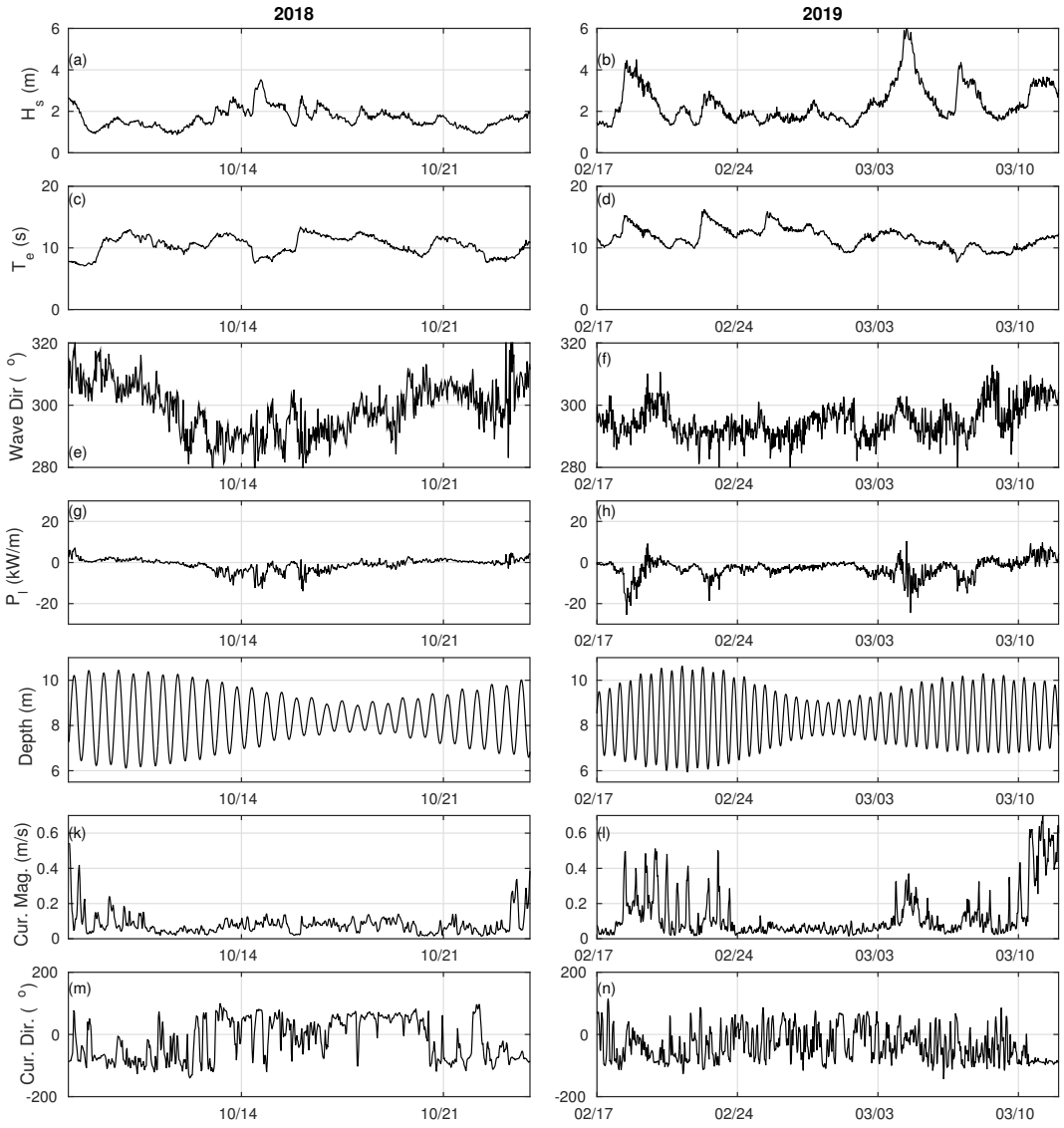

Figure 3. Field conditions during the 2018 (left-hand panels) and 2019 (right-hand panels) deployments. (**a**,**b**) Significant wave height; (**c**,**d**) energetic wave period; (**e**,**f**) mean wave direction (>300° Northward, <300° Southward); (**g**,**h**) longshore wave power; (**i**,**j**) measurement depth; (**k**,**l**) 2-h-averaged current magnitude and (**m**,**n**) direction against the headland projected into a cross-shore/alongshore local reference frame (>0 Northward, <0 Southward).

3. Results

3.1. Headland Rip Flow

This large range of tide/wave forcing conditions resulted in a large variability in headland rip current activity (Figure 3m,n). Periods of a few days with no rip activity are observed, with magnitude of depth-averaged flow below ≈0.1 m/s, readily coinciding with periods with $H_s < 2$ m. Long periods of rip flow activity are also observed, coinciding with periods of waves with $H_s > 2$ m and/or with oblique incidence with a preferred northern incidence ($P_l > 0$, deflection rip configuration), with no apparent influence of wind conditions. Time- and depth-averaged rip flow speed reached 0.6 m/s (Figure 3l). This peak does not coincide with the H_s peak on 5 March 2019, but with the peak of positive longshore power observed on 11 March 2019, highlighting the importance of wave incidence. When active, the rip flow direction is well-defined within the 270–290° (nautical convention) sector, meaning that the rip flows offshore along the headland with a slight westward inflexion. Results

also show that, when active, rip flow velocity is strongly modulated by the tide, with rip flow speed maximized for lower tides, while the flow direction is not readily affected.

Figure 4 provides insight into the relationship between the cross-shore/longshore components of the headland rip current and the longshore power P_l, which allows identifying the conditions for the deflection rip development. Following the basic conceptual scheme presented in Figure 1, a deflection rip is expected for positive longshore power ($P_l > 0$) corresponding to waves coming from the north. For these deflection rip configurations, rip flow speed strongly increases and deviates westward with increasing P_l. Results also suggest that rip flow activity increases with decreasing tidal elevation (Figure 4b) and offshore wave height (Figure 4d). Figure 5 further shows that tide modulation depends on incident wave energy. For $H_s < 3$ m, deflection rip is active only between low- and mid-tide, with maximum activity around mean low water level (Figure 5a,b). Tidal modulation disappears for high-energy waves (Figure 5c) when rip flow activity is maintained even for higher tide elevation (e.g., see from 11 March 2019 in Figure 3n).

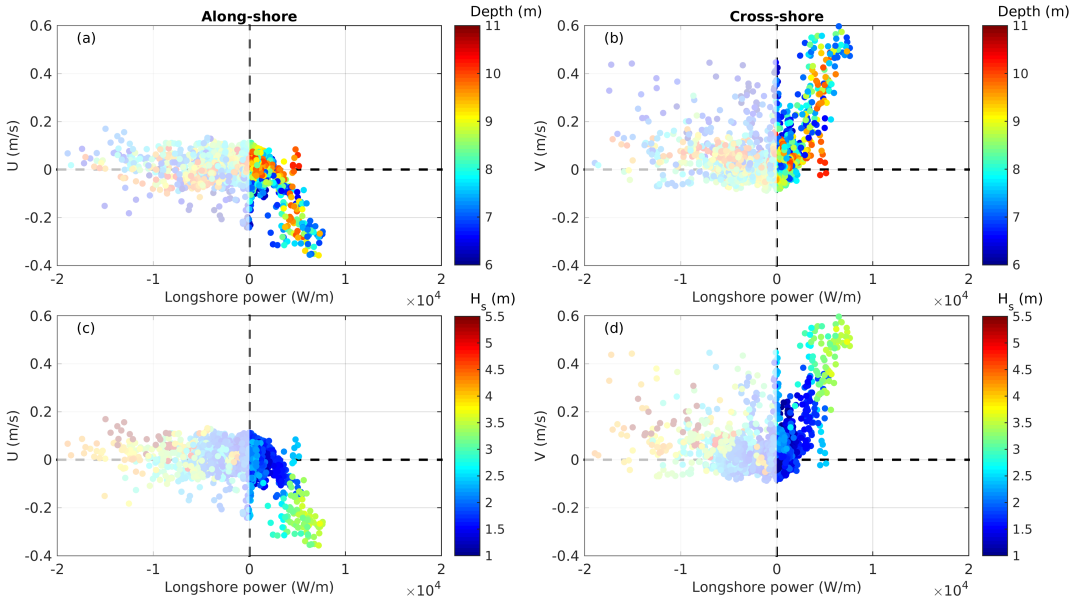

Figure 4. Scatter plot of depth-averaged and 2-h-averaged alongshore (**a**,**c**) and cross-shore (**b**,**d**) flow components against longshore power P_l. Positive/negative longshore power corresponds to northern/southern waves, positive/negative alongshore velocity component U corresponds to northward/southward current and positive/negative velocity component V corresponds to off/onshore flow. In the top and bottom panels the water depth and significant wave height are colored, respectively. The present analysis focuses on the deflection regime for $P_l > 0$ (right parts of the subplots).

3.2. Representative Rip Flow Events

Results show that the longshore wave power dictates the rip flow regime, with additional influence of wave height and tidal elevation. To explore the detailed rip flow response, two representative events in moderate- and high-energy deflection configuration were selected and further analyzed below in terms of temporal and vertical structure.

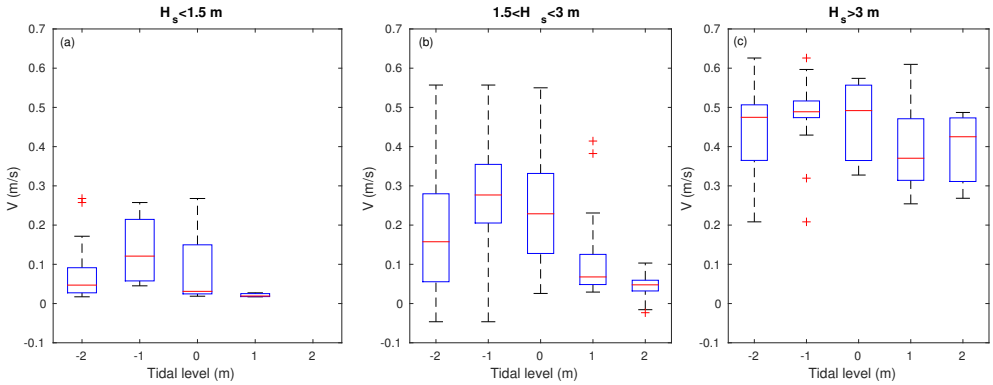

Figure 5. Boxplot for cross-shore velocity V with respect to the tidal elevation for deflection regime ($P_l > 0$). Data are processed into successive 1-m tidal elevation box, from -2.5 to 2.5 m, for three ranges of wave conditions: (**a**) $H_s < 1.5$ m, (**b**) $1.5 < H_s < 3$ m and (**c**) $H_s > 3$ m. In each boxplot, the horizontal red line is the median and the y-limits of the box are the 25th and 75th percentiles while the red crosses are outliers.

3.2.1. Moderate-Energy Deflection Rip

This event on 23 October 2018 (Figure 6) is characterized by an average wave height, period and direction of 1.6 m, 7.8 s and 322°, respectively, for the 2-h low-tide burst ($SWL = -1.5$ m, left-hand panels in Figure 6) and 1.7 m, 8.5 s and 314°, respectively, for the 2-h high-tide burst ($SWL = 1.4$ m, right-hand panels in Figure 6). At high tide, the headland rip is not active with both 2-min averaged flow components well below 0.1 m/s. By contrast, the headland rip is active at low tide with an offshore-directed velocity averaging around 0.2 m/s despite the fact that the current profiler was sitting in approximately 7-m water depth and located far offshore of the outer surf zone edge. The 2-min averaged cross-shore flow velocity also shows a striking pulsing behavior, with an energy peak at 0.00067 Hz, corresponding to very low frequency (VLF) motions with a dominant period of approximately 25 min (Figure 6c). The mean cross-shore current is also highly variable across the water column, with mean flow velocity almost linearly increasing from 0 near the bottom to approximately 0.3 m/s near the surface. By contrast, the alongshore component of the rip current shows pulsations at a wider and shorter range of periods and is nearly depth-uniform.

3.2.2. High-Energy Deflection Rip

This event on 10 March 2019 is characterized by an average wave height, period and direction of 3.5 m, 10.8 s and 302°, respectively, for the 2-h low-tide burst ($SWL = -1.6$ m, left-hand panels in Figure 7) and 3.5 m, 11.5 s and 305°, respectively, for the 2-h high-tide burst ($SWL = 1.3$ m, right-hand panels in Figure 7). In contrast with the previous event, the headland rip is active at both low and high tide, with a time- and depth-averaged offshore-directed velocity of approximately 0.5 m/s and 0.3 m/s, respectively. At low tide the current meter is in approximately 7.1-m depth and is therefore located within the outer surf zone. Both the 2-min averaged alongshore and cross-shore flow velocity components show a strong pulsing behavior, with energy peaks at approximately 0.00069 and 0.00041 Hz, corresponding to very low-frequency motions with a dominant period of approximately 24 and 40 min for along and cross-shore components, respectively. At high tide, lower frequency pulsing is also observed with a more pronounced cross-shore pulsation than for low tide. Both components are fluctuating in the same frequency band (about 0.00041 Hz, i.e., 40 min). The rip flow is also more depth variable at high tide, when the currentmeter is located well offshore of the surf zone edge. In contrast with the low tide situation of the moderate-energy deflection rip described previously, here both the cross-shore and alongshore components are depth variable, with mean flow velocity roughly linearly increasing from the bottom to the surface where it almost reaches 0.5 m/s. At low tide the current profile is nearly depth uniform, with the development of an (incomplete) bottom boundary layer.

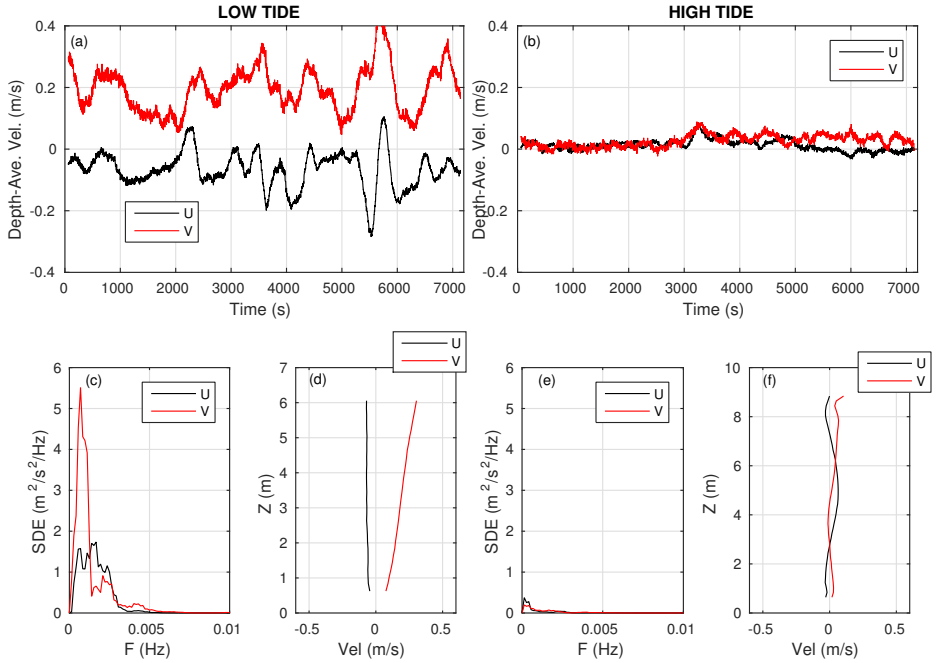

Figure 6. Moderate-energy deflection rip event on 23 October 2018 at low (left-hand panels) and high (right-hand panels) tide with cross-shore ($V > 0$ for westward current) and alongshore ($U > 0$ for northward current) depth-averaged velocity components in red and black, respectively. (**a**,**b**) 2-h burst of 2-min moving averaged velocities; (**c**,**e**) spectral density of energy; (**d**,**f**) burst-averaged velocity profiles.

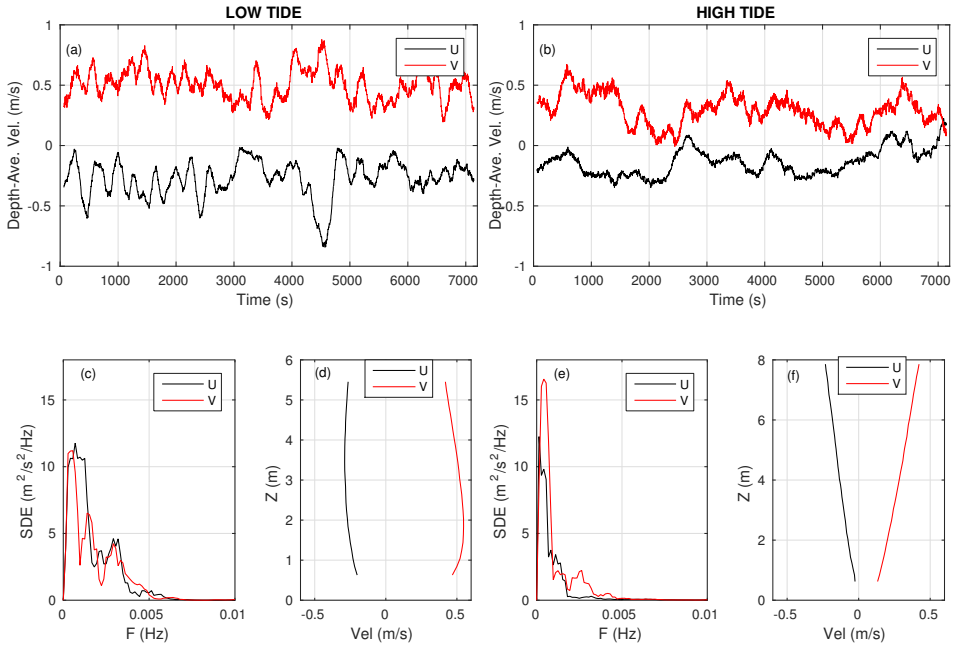

Figure 7. High-energy deflection rip on 10 March 2019 at low (left-hand panels) and high (right-hand panels) tide with cross-shore and alongshore depth-averaged velocity components in red and clack, respectively. (**a**,**b**) 2-h burst of 2-min moving averaged velocities; (**c**,**e**) spectral density of energy; (**d**,**f**) burst-averaged velocity profiles.

4. Discussion

The above analysis emphasizes the complex and contrasting behaviors that headland rips can exhibit in high-energy meso-macro tidal settings. In particular, the primary driving mechanism of headland rip is critical to rip flow activity. Our results indicate that headland rips driven by the deflection of the alongshore current against the structure are the most intense. In addition, this type of rip was the only one for which offshore-directed depth- and time-averaged velocities were measured far beyond the surf zone. This is in line with previous modeling work [29] and drifter measurements [17] in lower energy environments showing that mean flow speed and exit rates are both greater under deflection rip configuration than under shadow rip configurations, with the latter often dominated by a circulatory flow regime [27]. It is therefore hypothesized that boundary rips driven by the deflection of the alongshore current can be a dominant mechanism for water and sediment exchanges between the embayed beach and the inner-shelf and/or the adjacent embayments.

The present study also indicates that deflection rip flow speed consistently increases with increasing longshore wave power. However, it is expected to eventually saturate as offshore wave height further increases. Scott et al. [16] showed that if the ratio of the headland length to the surf zone width decreases below 1.25 the amount of deflected alongshore current decreases. This means that as offshore wave height further increases with the surf zone edge reaching or exceeding the headland tip, the amount of deflected current does not further increase. It must be noted that this 2018/2019 winter was characterized by the absence of a severe storm, with the most energetic event captured with $H_s \approx 6.5$ m and near-shore normal incidence, thus preventing exploration of a potential saturation of deflection rip velocity as offshore wave height further increases. Additional deployments and/or modeling experiments will be required to address rip flow characteristics during severe storms ($H_s > 8$ m), for which waves break well offshore of the headland at PCA.

Headland rips have received little attention so far compared to, for instance, channel rips. While tide modulation of channel rips has been documented fairly well, showing, most of the time, maximized rip flow activity around lower tide levels (e.g., [32–34]), tidal modulation of headland rips has never been explored. Similar behavior to channel rips is observed at PCA for moderate-wave energy conditions during which the deflection rip is only active at low tide (Figure 6). Although one can expect that at high tide the current meter was located too far away from the rip, resulting in a biased tide modulation, a drifter experiment conducted that day confirms that maximum headland rip flow activity was observed at low tide [40], in line with the measurements collected by our current meter. Although slight tidal modulation was also observed for the high-energy deflection rip event shown in Figure 7, on average no clear tidal modulation was observed (Figure 5c). Interestingly enough, for high-energy conditions it is expected that deflection rip flow becomes maximum at high tide. Steeper surf zone slope and more prominent offshore extent of the headland as the entire surf zone migrates landward should result in more alongshore current to be deflected [16]. This will need to be further explored using numerical modeling and/or denser Eulerian measurements against the headland, in order to capture a much wider wave height/longshore power spectrum. Previous work also indicates that, in the laboratory and for highly alongshore non-uniform bar bathymetry, the vertical profile of channel rips varies from depth-uniform in the rip neck to depth-varying further offshore in the rip head [41]. Such vertical structure of the rip flow has never been measured in the field, because of the lack of velocity profile measurements in the neck and the head of the rip, and also because the horizontal dimensions of rip circulation are large compared to the surf zone water depth. This statement does not stand for the deflection rips observed at PCA. As deflection rips consist in narrow jets extending well beyond the surf zone in deeper water (>10 m), the vertical dimension becomes non-negligible. Here, using the wave and tide modulation of the surf zone location as a proxy to study the spatial structure of the rip we found that, in line with the laboratory work on channel rips, the deflection rip flow is nearly depth-uniform in the neck and becomes increasingly sheared seaward through the rip head (Figure 7).

Deflection rips are associated with large VLF fluctuations, with periods ranging 10–60 min. The VLF motions with periods > 30 min, which is much longer than VLF motions typically observed in various rip current systems (e.g., [42–44]), are closer to the recent observation of Elgar et al. [45] who referred to these surf zone eddy motions to as extremely low-frequency motions (ELF). The relationships between wave/tide forcing conditions, the mechanism of boundary rip generation, and VLF flow response was further analyzed. Significant amplitudes of VLF fluctuations were systematically computed over successive 2-h bursts, integrating the spectral density of variance for velocity (along-shore, cross-shore and magnitude), and plotted against mean flow velocities, tide elevation and longshore wave power. The selected frequency band was $0.0002 < F < 0.0033$ Hz, i.e., to account for periods between 5 min and 1h20, in line with the observed dominant VLF/ELF motions. Figure 8 shows a clear discrimination between deflection (reddish bubbles) and shadow (yellow-blue bubbles) configurations. For deflection rips, the VLF/ELF motions of the cross-shore component increases with increasing mean cross-shore component ($r^2 = 0.62$). The correlation is also significant for the alongshore component ($r^2 = 0.55$) and particularly for the flow magnitude ($r^2 = 0.8$). This correlation indicates that the VLF/ELF motions are related to the shear instabilities of the rip current, as an increase in velocity shear should increase instability intensities. This contrasts with previous observations of channel rips showing that VLF amplitude is poorly correlated with the mean flow speed but more significantly correlated with incident wave energy [42]. The cut-off frequency between infragravity and VLF bands is typically set arbitrarily to values such as 0.004 or 0.005 Hz, or even 0.008 Hz [46]. Given the long wave periods (up to 16 s) that were encountered during our measurement periods, it is likely that some infragravity energy has been taken into account in Figure 8. However, computations using other upper-frequency limits, e.g., $F = 0.0083$ Hz and $F = 0.0017$ Hz, corresponding to periods of 2 and 10 min, showed similar outcomes to the results discussed here. At this stage the underlying mechanism driving these VFL and ELF flow motions is unclear and should be further investigated through detailed process-based modeling.

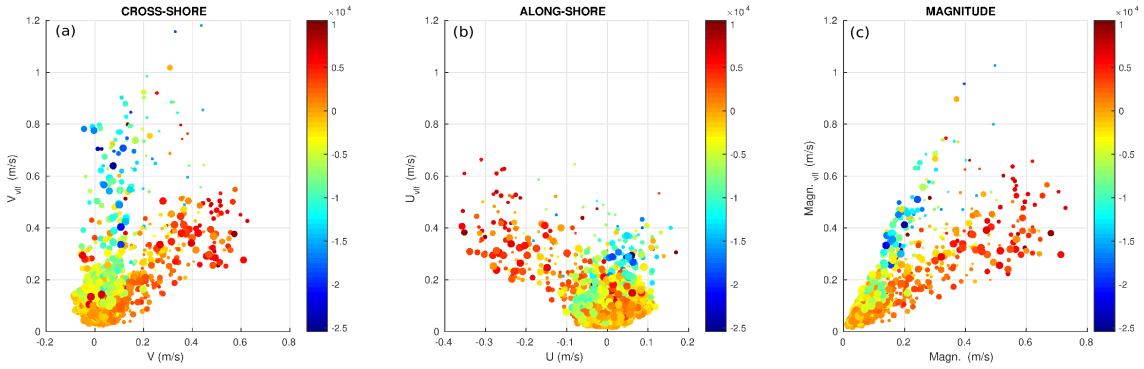

Figure 8. Significant amplitude of very low frequency (VLF) fluctuations (above 5min period) vs mean current for the cross-shore (**a**) and along-shore (**b**) components and magnitude (**c**) for the depth-averaged velocity. Longshore power and tidal elevation are depicted by color levels and marker size (the larger, the higher), respectively.

5. Conclusions

The present study used 42 days of velocity profile measurements collected from one current profiler along a natural headland at PCA beach, southwest France, in order to study headland rip activity. The current meter was alternatively located in the rip neck, rip head or away from the rip as wave and tide conditions changed. Strong headland rips driven by the deflection of the alongshore current against the headland were observed, associated with large offshore-directed velocities and tide modulation. Deflection rip flow structure varied from nearly depth-uniform in the rip neck to strongly depth-varying further offshore in the rip head with maximum velocities near the surface. VLF motions of the rip flow were strong, with periods ranging 10–60 min and a dominant peak period about 40 min,

i.e., extending in the ELF range defined by Elgar et al. [45]. The velocities measured in this study (up to 0.6 m/s in $>$ 10-m depth under $<$ 4 m obliquely incident waves) confirm that, by contrast to undertow, deflection rips can potentially transport large quantities of sediment offshore well beyond the depth of closure, which is estimated to be approximately 14 m at this site [40], as storm waves can well exceed 8 m. Such a dataset provides new insight into headland rips as a dominant mechanism for water and sediment exchanges between the embayed beach and the inner-shelf and/or the adjacent embayments.

Author Contributions: Conceptualization, D.S., B.C. and P.B.; methodology, D.S., B.C. and P.B.; investigation, D.S., B.C, A.M. and P.B.; resources, D.S., B.C. and P.B.; data curation, D.S. and B.C.; writing—original draft preparation, D.S. and B.C.; writing—review and editing, D.S., B.C., A.M. and P.B.; visualization, D.S. and B.C.; supervision, D.S.; project administration, D.S. and P.B.; funding acquisition, D.S. And P.B. All authors have read and agreed to the published version of the manuscript.

Funding: This research was funded by CNRS-INSU (EC2CO PANACHE) and Region Nouvelle Aquitaine (contract n°2017-1R20107), project MEPELS (contract n°18CP05 - DGA/Shom) and SNO Dynalit labeled by CNRS-INSU.

Acknowledgments: PCA is a monitoring site of SNO Dynalit providing long-term support. B.C. funded by project SONO (grant number ANR-17-CE01-0014). The Gladys group provided support to the experimentation. The wave buoy data are publicly available through the French Candhis network operated by CEREMA.

Conflicts of Interest: The authors declare no conflict of interest.

References

1. Short, A.D.; Masselink, G. Embayed and structurally controlled beaches. In *Handbook of Beach and Shoreface Morphodynamics*; Wiley: New York, NY, USA, 1999; pp. 230–250.
2. Silva, R.; Baquerizo, A.; Ángel Losada, M.; Mendoza, E. Hydrodynamics of a headland-bay beach—Nearshore current circulation. *Coast. Eng.* **2010**, *57*, 160–175. [CrossRef]
3. Valiente, N.G.; McCarroll, R.J.; Masselink, G.; Scott, T.; Wiggins, M. Multi-annual embayment sediment dynamics involving headland bypassing and sediment exchange across the depth of closure. *Geomorphology* **2019**, *343*, 48–64. [CrossRef]
4. Gallop, S.; Bryan, K.; Coco, G.; Stephens, S. Storm-driven changes in rip channel patterns on an embayed beach. *Geomorphology* **2011**, *127*, 179–188. [CrossRef]
5. Castelle, B.; Coco, G. The morphodynamics of rip channels on embayed beaches. *Cont. Shelf Res.* **2012**, *43*, 10–23. [CrossRef]
6. Harley, M.D.; Turner, I.L.; Short, A.D. New insights into embayed beach rotation: The importance of wave exposure and cross-shore processes. *J. Geophys. Res. Earth Surf.* **2015**, *120*, 1470–1484. [CrossRef]
7. Robinet, A.; Castelle, B.; Idier, D.; Harley, M.; Splinter, K. Controls of local geology and cross-shore/longshore processes on embayed beach shoreline variability. *Mar. Geol.* **2020**, *422*, 106118. [CrossRef]
8. Harley, M.; Andriolo, U.; Armaroli, C.; Ciavola, P. Shoreline rotation and response to nourishment of a gravel embayed beach using a low-cost video monitoring technique: San Michele-Sassi Neri, Central Italy. *J. Coast. Conserv.* **2014**, *18*, 551–565. [CrossRef]
9. Masselink, G.; Pattiaratchi, C. Seasonal changes in beach morphology along the sheltered coastline of Perth, Western Australia. *Mar. Geol.* **2001**, *172*, 243–263. [CrossRef]
10. Klein, A.; Benedet, L.; Schumacher, D. Short-term beach rotation processes in distinct headland bay beach systems. *J. Coast. Res.* **2002**, *18*, 442–458.
11. Ojeda, E.; Guillén, J. Shoreline dynamics and beach rotation of artificial embayed beaches. *Mar. Geol.* **2008**, *253*, 51–62. [CrossRef]
12. Ranasinghe, R.; McLoughlin, R.; Short, A.; Symonds, G. The Southern Oscillation Index, wave climate, and beach rotation. *Mar. Geol.* **2004**, *204*, 273–287. [CrossRef]
13. Loureiro, C.; Ferreira, O.; Cooper, J.A.G. Geologically constrained morphological variability and boundary effects on embayed beaches. *Mar. Geol.* **2012**, *329–331*, 1–15. [CrossRef]
14. Turki, I.; Medina, R.; Coco, G.; Gonzalez, M. An equilibrium model to predict shoreline rotation of pocket beaches. *Mar. Geol.* **2013**, *346*, 220–232. [CrossRef]
15. Ratliff, K.M.; Murray, A.B. Modes and emergent time scales of embayed beach dynamics. *Geophys. Res. Lett.* **2014**, *41*, 7270–7275. [CrossRef]

16. Scott, T.; Austin, M.; Masselink, G.; Russell, P. Dynamics of rip currents associated with groynes—Field measurements, modelling and implications for beach safety. *Coast. Eng.* **2016**, *107*, 53–69. [CrossRef]
17. McCarroll, R.J.; Brander, R.W.; Turner, I.L.; Power, H.E.; Mortlock, T.R. Lagrangian observations of circulation on an embayed beach with headland rip currents. *Mar. Geol.* **2014**, *355*, 173–188. [CrossRef]
18. Castelle, B.; Scott, T.; Brander, R.; McCarroll, R. Rip current types, circulation and hazard. *Earth-Sci. Rev.* **2016**, *163*, 1–21. [CrossRef]
19. da Silva, G.V.; Toldo, E.E.; da F. Klein, A.H.; Short, A.D.; Woodroffe, C.D. Headland sand bypassing—Quantification of net sediment transport in embayed beaches, Santa Catarina Island North Shore, Southern Brazil. *Mar. Geol.* **2016**, *379*, 13–27. [CrossRef]
20. Goodwin, I.D.; Stables, M.A.; Olley, J.M. Wave climate, sand budget and shoreline alignment evolution of the Iluka–Woody Bay sand barrier, northern New South Wales, Australia, since 3000 yr BP. *Mar. Geol.* **2006**, *226*, 127–144. [CrossRef]
21. Coutts-Smith, A.J. The Significance of Mega-Rips Along an Embayed Coast. Ph.D. Thesis, University of Sydney, Sydney, Australia, 2004.
22. Dalrymple, R.A.; MacMahan, J.H.; Reniers, A.J.; Nelko, V. Rip Currents. *Annu. Rev. Fluid Mech.* **2011**, *43*, 551–581. [CrossRef]
23. Loureiro, C.; Ferreira, O.; Cooper, J.A.G. Extreme erosion on high-energy embayed beaches: Influence of megarips and storm grouping. *Geomorphology* **2012**, *139–140*, 155–171. [CrossRef]
24. McCarroll, R.J.; Brander, R.W.; Turner, I.L.; Leeuwen, B.V. Shoreface storm morphodynamics and mega-rip evolution at an embayed beach: Bondi Beach, NSW, Australia. *Cont. Shelf Res.* **2016**, *116*, 74–88. [CrossRef]
25. McCarroll, R.J.; Masselink, G.; Valiente, N.G.; Scott, T.; King, E.V.; Conley, D. Wave and Tidal Controls on Embayment Circulation and Headland Bypassing for an Exposed, Macrotidal Site. *J. Mar. Sci. Eng.* **2018**, *6*, 94. [CrossRef]
26. Valiente, N.G.; Masselink, G.; Scott, T.; Conley, D.; McCarroll, R.J. Role of waves and tides on depth of closure and potential for headland bypassing. *Mar. Geol.* **2019**, *407*, 60–75. [CrossRef]
27. Pattiaratchi, C.; Olsson, D.; Hetzel, Y.; Lowe, R. Wave-driven circulation patterns in the lee of groynes. *Cont. Shelf Res.* **2009**, *29*, 1961–1974. [CrossRef]
28. Gallop, S.L.; Bryan, K.R.; Pitman, S.J.; Ranasinghe, R.; Sandwell, D.R.; Harrison, S.R. Rip current circulation and surf zone retention on a double barred beach. *Mar. Geol.* **2018**, *405*, 12–22. [CrossRef]
29. Castelle, B.; Coco, G. Surf zone flushing on embayed beaches. *Geophys. Res. Lett.* **2013**, *40*, 1–5. [CrossRef]
30. Wind, H.G.; Vreugdenhil, C.B. Rip-current generation near structures. *J. Fluid Mech.* **1986**, *171*, 459–476. [CrossRef]
31. Mouragues, A.; Bonneton, P.; Castelle, B.; Marieu, V.; Barrett, A.; Bonneton, N.; Detand, G.; Martins, K.; McCarroll, R.; Morichon, D.; et al. Field observations of wave-induced headland rips. *J. Coast. Res.* **2020**. [CrossRef]
32. Brander, R.W.; Short, A.D. Flow kinematics of low-energy rip current systems. *J. Coast. Res.* **2001**, *17*, 468–481.
33. Austin, M.; Scott, T.; Brown, J.; Brown, J.; MacMahan, J.; Masselink, G.; Russell, P. Temporal observations of rip current circulation on a macro-tidal beach. *Cont. Shelf Res.* **2010**, *30*, 1149–1165. [CrossRef]
34. Bruneau, N.; Bonneton, P.; Castelle, B.; Pedreros, R. Modeling rip current circulations and vorticity in a high-energy meso-macrotidal environment. *J. Geophys. Res.* **2011**, *116*. [CrossRef]
35. Castelle, B.; Dodet, G.; Masselink, G.; Scott, T. A new climate index controlling winter wave activity along the Atlantic coast of Europe: The West Europe Pressure Anomaly. *Geophys. Res. Lett.* **2017**, *44*, 1384–1392. [CrossRef]
36. Abadie, S.; Butel, R.; Dupuis, H.; Brière, C. Paramètres statistiques de la houle au large de la côte sud-aquitaine. *C. R. Geosci.* **2005**, *337*, 769–776. [CrossRef]
37. Brière, C. Etude de l'hydrodynamique d'une zone côtière anthropisée: l'embouchure de l'Adour et les plages adjacentes d'Anglet. Ph.D. Thesis, Université de Pau et des Pays de l'Adour, Pau, France, 2005.
38. Huguet, J.R.; Castelle, B.; Marieu, V.; Morichon, D.; de Santiago, I. Shoreline-Sandbar Dynamics at a High-Energy Embayed and Structurally-Engineered Sandy Beach: Anglet, SW France. *J. Coast. Res.* **2016**, *75*, 393–397. [CrossRef]
39. Rodriguez-Padilla, I.; Castelle, B.; Marieu, V.; Morichon, D. A Simple and Efficient Image Stabilization Method for Coastal Monitoring Video Systems. *Remote Sens.* **2019**, *12*, 70. [CrossRef]

40. Mouragues, A.; Bonneton, P.; Castelle, B.; Marieu, V.; McCarroll, R.; Scott, T.; Sous, D. New insights into high-energy surf zone currents and headland rips at a geologically-constrained mesotidal beach. *J. Geophys. Res. Oceans* in revision, 2020.
41. Haas, K.A.; Svendsen, I.A. Laboratory measurements of the vertical structure of rip currents. *J. Geophys. Res. Ocean.* **2002**, *107*, 15-1–15-19. [CrossRef]
42. MacMahan, J.H.; Reniers, A.J.H.M.; Thornton, E.B.; Stanton, T.P. Surf zone eddies coupled with rip current morphology. *J. Geophys. Res.* **2004**, *109*. [CrossRef]
43. Bruneau, N.; Castelle, B.; Bonneton, P.; Pedreros, R.; Almar, R.; Bonneton, N.; Bretel, P.; Parisot, J.P.; Sénéchal, N. Field observations of an evolving rip current on a meso-macrotidal well-developed inner bar and rip morphology. *Cont. Shelf Res.* **2009**, *29*, 1650–1662. [CrossRef]
44. Geiman, J.D.; Kirby, J.T. Unforced Oscillation of Rip-Current Vortex Cells. *J. Phys. Oceanogr.* **2013**, *43*, 477–497. [CrossRef]
45. Elgar, S.; Raubenheimer, B.; Clark, D.B.; Moulton, M. Extremely Low Frequency (0.1 to 1.0 mHz) Surf Zone Currents. *Geophys. Res. Lett.* **2019**, *46*, 1531–1536. [CrossRef]
46. Sous, D.; Tissier, M.; Rey, V.; Touboul, J.; Bouchette, F.; Devenon, J.L.; Chevalier, C.; Aucan, J. Wave transformation over barrier reefs. *Cont. Shelf Res.* **2019**. [CrossRef]